Nano Research

Open Access

Research Article

Tailoring the proximity of iron and manganese atomic sites for efficient CO_2 electroreduction reaction

Xiaohui Sun[1], Bangyan Zhang[1], Qing Lu[4], Jingjing Jiang[5], Chenliang Ye[2], Guoqing Cui[1], Zechao Zhuang[2], Jun Zhang[4], Johannes H. Bitter[3], Guanna Li[3], and Chunming Xu[1]

[1] State Key Laboratory of Heavy Oil Processing, China University of Petroleum (Beijing), Beijing 102249, China
[2] Department of Chemistry, Tsinghua University, Beijing 100084, China
[3] Biobased Chemistry and Technology, Wageningen University & Research, Wageningen, 6708WG, The Netherlands
[4] Department of Materials Science and Engineering, China University of Petroleum (East China), Qingdao 266580, China
[5] Institute of Analysis and Testing, Institute of Analysis and Testing, Beijing Academy of Science and Technology (Beijing Center for Physical and Chemical Analysis), Beijing 100094, China

Cite this article: *Nano Research*, **2025**, *18*, 94907249. https://doi.org/10.26599/NR.2025.94907249

ABSTRACT: Electrochemical carbon dioxide reduction reaction (CO_2RR) into high-value added chemicals and fuels has aroused wide attention, but suffers from high overpotential and poor selectivity. Herein, nitrogen-doped carbon supported Fe and Mn heteronuclear single atom catalysts with different Fe and Mn inter-site distance were fabricated via a templating isolation approach and tested for CO_2RR to CO in an aqueous solution. The catalyst with atomically dispersed Fe and Mn sites in close proximity exhibited the highest CO_2RR performance, with a CO Faradaic efficiency of 96% at a low overpotential of 320 mV, and a Tafel slope of only 62 mV·dec^{-1}, comparable to state-of-the-art gold catalysts. Experimental analysis combined with theory highlighted that single Mn atom at the neighboring site of Fe enhanced the electronic localization of Fe center, which facilitated the generation of key *COOH intermediate as well as CO* desorption on Fe, leading to superior CO_2RR performance at low overpotentials. This work offers atomic-level insights into the correlation between the inter-site distance of atomic sites and CO_2RR performance, and paves a new avenue for precise control of single-atom sites on carbon surface for highly active and selective electrocatalysts.

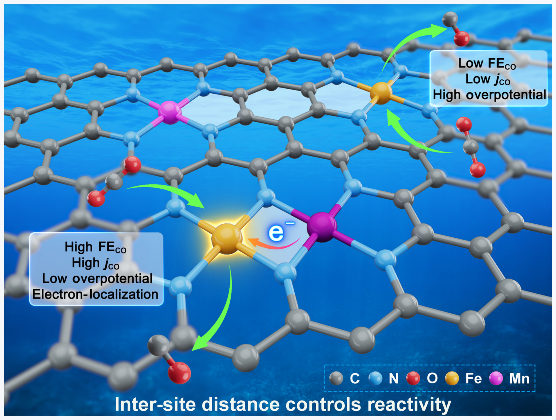

KEYWORDS: CO_2 electroreduction, heteronuclear single-atom catalyst, inter-site distance, electron localization, scaling relationships, low overpotentials

1 Introduction

Electrochemical carbon dioxide reduction reaction (CO_2RR) with renewable electricity is an eco-friendly approach to reverse global warming by decreasing atmospheric CO_2 levels [1–3]. Among the different reduction products (e.g., CO, HCOOH, CH_4 and CH_3OH, etc.), CO is an important feedstock to generate clean fuels with H_2 via Fischer–Tropsch synthesis [4, 5]. Because of the chemical inertness of CO_2, a high reduction potential is necessary to cleave the C–O bond [6–8]. Yet, hydrogen evolution reaction (HER) is kinetically dominated under such circumstance, which causes a loss to the CO selectivity and energetic utilization [9–12]. Hence, the design of robust and efficient CO_2RR electrocatalysts at low potentials is attractive but still a challenging task.

Gold nanoparticles (AuNPs) are highly active to produce CO at low potentials, while other earth-abundant metals (e.g., Fe, Co, Ni, etc.) are more selective for HER [13–15]. Downsizing transition-metal NPs to their atomic scale has exhibited huge potential in CO_2RR, and the distinct activity for CO production is strongly dependent upon the nature of single atom site [16–19]. For example, atomically dispersed M-N_4 (M = Fe, Co, Ni, Mn, etc.) moieties in carbon matrix have showed high CO Faradaic efficiency

---

Received: December 13, 2024; **Revised:** January 6, 2025
Accepted: January 9, 2025

Address correspondence to Xiaohui Sun, sunxiaohui@cup.edu.cn; Chenliang Ye, chenliangye@ncepu.edu.cn; Guanna Li, guanna.li@wur.nl

(FE) in a wide potential range [20–24]. However, the intrinsic activities of these single-atom catalysts (SACs) at low potentials are still far below state-of-the-art AuNPs. In principle, an eligible electrocatalyst for CO_2RR to CO should not only bind the COOH* intermediate strongly enough to facilitate CO_2 activation, but interact weakly with CO* for fast desorption from the surface [25, 26]. Thus, modulating the electronic structures of these atomic sites would be viable to boost their inherent activity at low potentials by altering the adsorption and desorption barriers of key intermediates.

Various factors are known to regulate the electronic states of atomically dispersed sites, including coordination number, local strain, vacancy, and inter-site distance, etc. [27–34]. Among them, the inter-site-distance effect has recently gained great interests, and doping a second metal atom into the original single-metal-site system represents peculiar advantages. Two single atoms in proximity cannot only provide two adjacent adsorption sites, but likely interact mutually to adjust their respective electronic structures [35–37]. Such regulation in electronic state is supposed to break the intrinsic adsorption–energy scaling relationship upon SACs, and hence promote the catalytic activity and selectivity. For instance, strong interactions between adjacent Fe-N_4 moieties with an inter-site distance less than 1.2 nm were proved to alter the electronic structure of Fe, resulting in an increased intrinsic activity in the oxygen reduction reaction [38]. A couple of adjacent single Cu-N_3 configurations were also found to promote the C-C coupling synergistically for the production of ethanol during CO_2RR compared to single Cu atoms in a long distance [39]. So far, heteronuclear single atoms in nitrogen-doped carbon (NC) matrix have been widely investigated in CO_2RR, such as Fe-Ni, Ni-Cu, Co-Zn, and Zn-Ln, etc. [40–45]. However, to the best of our knowledge, how the inter-site-distance between such heteronuclear single atom tailors their respective electronic structures and hence the CO_2RR performance is barely explored.

In this study, we propose a silica-templated isolation approach to design a series of nitrogen-doped carbon supported Fe and Mn heteronuclear single atom catalysts. By regulating the sequence between silica removal and Mn adsorption in Fe-SAC@NC, the distance between single Fe and Mn atoms can be precisely controlled. Moreover, such a stepwise design approach also enabled us to solely study how the Fe–Mn distance influenced CO_2RR by excluding the interference of possibly existed homonuclear isolated Fe_2 and Mn_2 sites. When these catalysts were tested in CO_2RR, the FeMn-SAC@NC with neighboring single Fe and Mn sites exhibited a high and stable CO FE (FE_{CO}) of 96% for at least 24 h at a low overpotential of 320 mV, far beyond the counterpart with Fe and Mn heteronuclear single atoms in a long distance (denoted as Fe/Mn-SAC@NC) as well as Fe-SAC@NC and Mn-SAC@NC. Experimental analysis combined with theory demonstrated that single Mn atom in the proximity, especially at the neighboring site of Fe increased the electron density of Fe center. The enhanced electron localization of single Fe site markedly boosted the generation of *COOH as well as the desorption of CO*, leading to superior CO_2RR performance at low overpotentials.

2 Results and discussion

FeMn-SAC@NC was fabricated via a stepwise approach (Fig. 1(a)): (1) Zeolitic imidazolate framework-8 (ZIF-8, $Zn(MIM)_2$, MIM = 2-methylimidazolate) consisting of large cavities (11.6 Å) and small windows (3.4 Å) was utilized as a host to encapsulate the iron source (iron(III) 2,4-pentanedionate, $Fe(acac)_3$, molecular diameter ca. 9.7 Å) to form $Fe(acac)_3$@ZIF-8; (2) a silica layer was then covered on $Fe(acac)_3$@ZIF-8 by hydrolysis of tetraethyl orthosilicate (TEOS) to produce $Fe(acac)_3$@ZIF-8@SiO_2; (3) pyrolysis of $Fe(acac)_3$@ZIF-8@SiO_2 and subsequent acid etching of silica were conducted to yield Fe-SAC@NC; (4) finally, a Mn(II)-phenanthroline complex was adsorbed into Fe-SAC@NC, and the mixture was pyrolyzed again to harvest FeMn-SAC@NC. For comparative study, Fe/Mn-SAC@NC with heteronuclear single Fe and Mn atoms in a long distance was also synthesized by reversing the order of silica etching and Mn(II)-phenanthroline complex adsorption (see supporting information for details) Transmission electron microscopy (TEM) analysis indicated that $Fe(acac)_3$@ZIF-8 exhibited a rhombic dodecahedron-like structure (Fig. 1(b)). After pyrolysis and SiO_2 leaching, FeMn-SAC@NC, Fe-SAC@NC and Mn-SAC@NC still reserved the shape of ZIF-8 but with some shrinkage (Fig. 1(c), and Figs. S1 and S2 in the Electronic Supplementary Material (ESM)). As for Fe/Mn-SAC@NC, a thin and highly porous layer was present on the surface of the internal dodecahedron, indicative of the core–shell structure (Fig. S3 in the ESM). No Fe and Mn nanoparticles were observed in these catalysts, while the elemental mapping analysis demonstrated a uniform distribution of C, N, Fe, and Mn elements throughout the representative FeMn-SAC@NC, highlighting the highly dispersed Fe and Mn species in the carbon matrix (Figs. 1(f)–1(i)). The aberration-corrected high-angle annular dark-field scanning TEM (HAADF-STEM) analysis was further carried out to recognize the Fe and Mn species. As shown in Fig. 1(d), some bright spots in the atomic range were observed in the representative FeMn-SAC@NC catalyst, demonstrating the atomically dispersed Fe and Mn. Moreover, most of these bright dots were found to be in a close distance, and even some of them appeared in pairs with an inter-site distance of 2.3 Å (Fig. 1(e)). Such phenomena directly manifested that single Fe and Mn atoms were to a large extent present in a short distance in FeMn-SAC@NC.

Powder X-ray diffraction (XRD) pattern of $Fe(acac)_3$@ZIF-8 matched well with ZIF-8, confirming the successful synthesis (Fig. S4 in the ESM) [46]. After pyrolysis and SiO_2 removal, only two reflections at 2θ = 24° and 44° were detected in FeMn-SAC@NC, Fe/Mn-SAC@NC, Fe-SAC@NC and Mn-SAC@NC, which were assigned to the (002) and (100) planes of carbon, respectively (Fig. S5 in the ESM) [47, 48]. No any metal (oxide) reflections were detected, in consistence with the TEM results. The graphitization degree of the carbon substrate for these as-synthesized catalysts was further analyzed by Raman spectroscopy. The characteristic D and G bands of carbon at 1350 and 1580 cm^{-1} were clearly observed, corresponding to graphitic disordered or defective carbon and sp^2-bonded graphitic carbon sheets, respectively (Fig. S6 in the ESM) [49]. The comparable intensity ratio between the two bands indicated a similar graphitization degree of the carbon support in these catalysts [50, 51]. The Fe and Mn loadings in FeMn-SAC@NC were 0.4 wt.% and 0.3 wt.%, according to the inductively coupled plasma-optical emission spectrometry (ICP-OES) analysis.

X-ray photoelectron spectroscopy (XPS) was used to identify the surface chemical states of FeMn-SAC@NC, Fe/Mn-SAC@NC, Fe-SAC@NC and Mn-SAC@NC. The N 1s signals were deconvoluted into five peaks at 398.2, 399.1, 399.8, 400.8 and 402.5 eV, corresponding to pyridinic-N, Fe/Mn-N coordination configurations, pyrrolic-N, quaternary-N and oxidized-N, respectively (Fig. 2(a), and Figs. S7 and Table S1 in the ESM) [52, 53]. As for the Fe 2p spectra in Fig. 2(b), the Fe $2p_{3/2}$ signals for

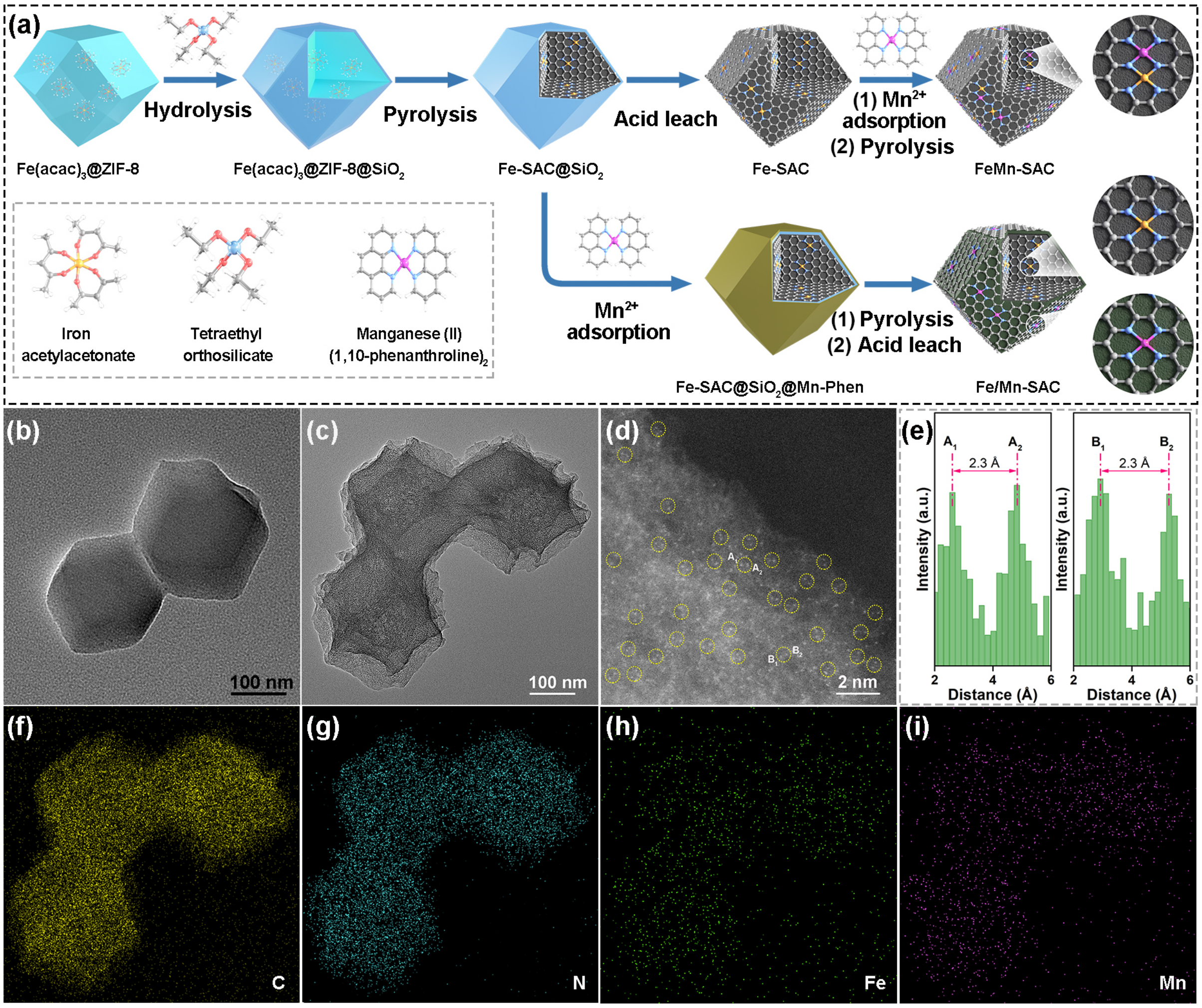

Figure 1 (a) Schematic illustration for the synthetic procedure of FeMn-SAC@NC and Fe/Mn-SAC@NC. TEM images of (b) Fe(acac)$_3$@ZIF-8 and (c) FeMn-SAC@NC. (d) HAADF-STEM image of FeMn-SAC@NC and (e) the corresponding Z-contrast analysis of regions A and B in (d). Energy dispersive spectroscopy (EDS) elemental mapping images of (f) C, (g) N, (h) Fe and (i) Mn in FeMn-SAC@NC.

FeMn-SAC@NC, Fe/Mn-SAC@NC and Fe-SAC@NC were situated between those of Fe^0 (706.7 eV) and Fe$_2$O$_3$ (711.6 eV), indicative of an electropositive Fe$^{\delta+}$ ($0 < \delta < 3$) [54, 55]. Similarly, positively charged Mn$^{\delta+}$ species ($0 < \delta < 3$) were also deduced in FeMn-SAC@NC, Fe/Mn-SAC@NC and Mn-SAC@NC by comparing their Mn 2p$_{3/2}$ signals with those of Mn^0 (638.4 eV) and Mn$_2$O$_3$ (641.8 eV), as shown in Fig. 2(c) [56, 57]. Interestingly, the valence states of Fe in three Fe containing catalysts decreased with the inter-site distance between Fe and Mn: FeMn-SAC@NC (710.1 eV) < Fe/Mn-SAC@NC (710.6 eV) < Fe-SAC@NC (710.9 eV), but for that of Mn in the Mn based samples, the trend was just the reverse: FeMn-SAC@NC (641.6 eV) > Fe/Mn-SAC@NC (641.2 eV) > Mn-SAC@NC (641.0 eV). Hence, owing to the higher electronegativity of Fe than Mn, single Mn atoms tended to donate more electrons to Fe in a short distance.

Fourier transformations-extended X-ray adsorption fine structure spectroscopy (EXAFS) was further conducted to obtain the local coordination information of Fe and Mn in these as-synthesized catalysts. As present in Fig. 2(d), in the k^2-whighted R space EXAFS of Fe K-edge, FeMn-SAC@NC, Fe/Mn-SAC@NC and Fe-SAC@NC exhibited their main peak at 1.44 Å without the emergence of the Fe–Fe scattering at 2.21 Å. Obviously, the existence of any metallic Fe nanoparticles was eliminated in these samples, and the Fe species were mainly present in an atomically dispersed state [58]. Similar phonomena were also observed for three Mn containing samples, and the absence of any Mn–Mn scattering at 2.30 Å highlighted the atomically dispersive feature of Mn species (Fig. 2(g)) [59, 60]. By fitting the EXAFS spectra of FeMn-SAC@NC, Fe/Mn-SAC@NC, Fe-SAC@NC and Mn-SAC/NC, the local structures of Fe and Mn in these catalysts were identified, in which each Fe and Mn atom was coordinated by four N atoms and one O atom (Figs. 2(e), 2(f), 2(h) and 2(i), and Figs. S8–S11 and Table S2 in the ESM).

After exploring the geometric and electronic structures of these as-synthesized catalysts, the CO$_2$ electrocatalytic performances were further measured by linear sweep voltammetry (LSV) in a three-electrode cell filled with CO$_2$-saturated 0.5 M KHCO$_3$ electrolyte (Fig. S12 in the ESM). No liquid products but only CO and H$_2$ were detected during CO$_2$RR (Fig. 3(a) and Fig. S13 in the ESM). Among these catalysts, FeMn-SAC@NC displayed the highest FE (FE$_{CO}$) and partial current density of CO (j_{CO}) over the potential window from −0.23 to −1.03 V (vs. reversible hydrogen electrode (RHE)) (Figs. 3(a) and 3(b)). Specifically, a FE$_{CO}$ of 96% accompanied with a current density (j) of 5 mA·cm^{-2} was achieved on FeMn-SAC@NC at a small overpotential of 320 mV, which outperformed most of the recently reported atomically dispersed metal catalysts

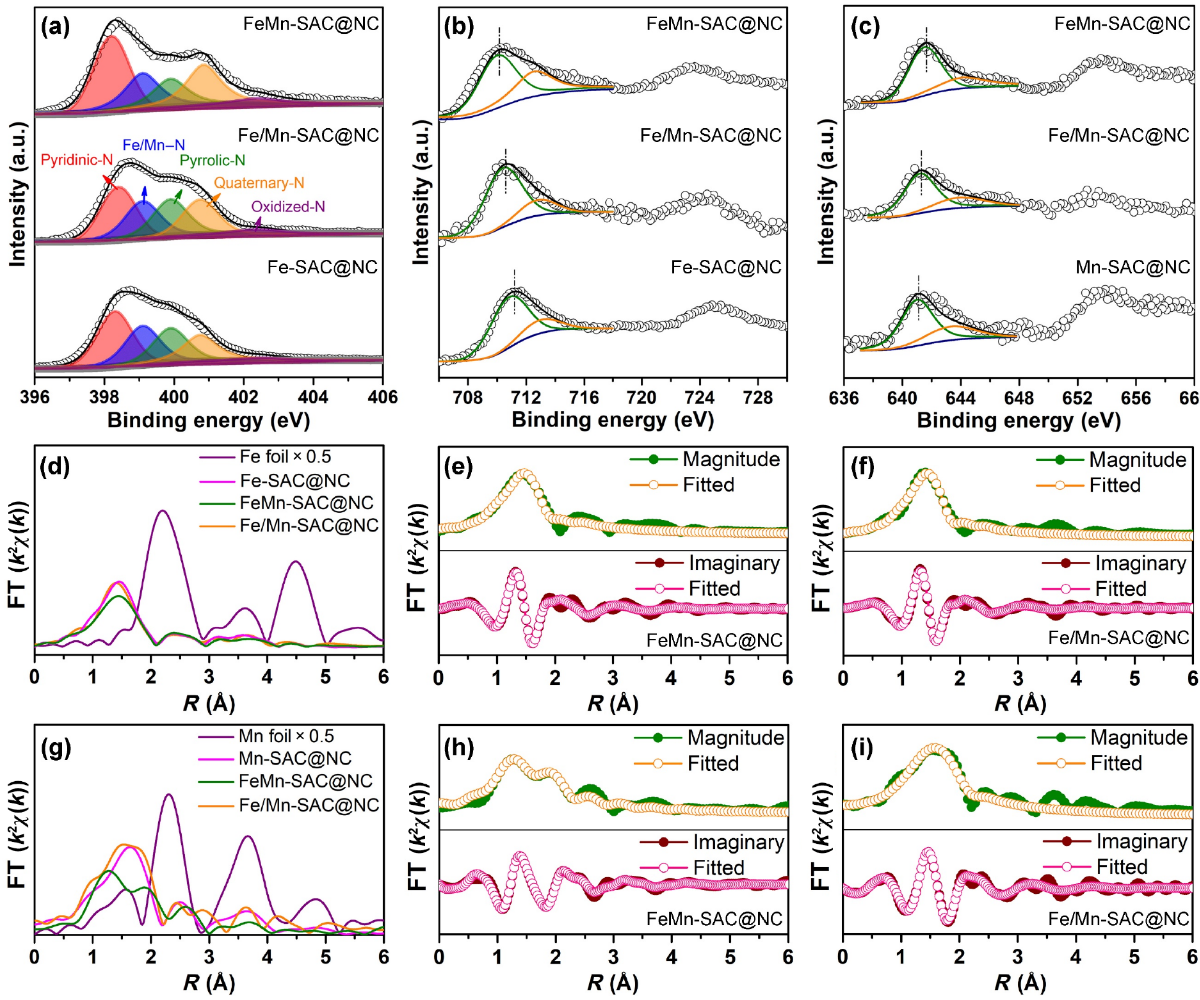

Figure 2 High-resolution (a) N 1s and (b) Fe 2p XPS of FeMn-SAC@NC, Fe/Mn-SAC@NC and Fe-SAC@NC. (c) High-resolution Mn 2p XPS of FeMn-SAC@NC, Fe/Mn-SAC@NC and Mn-SAC@NC. (d) Fourier transform (FT) of the k^2-weighted EXAFS spectra at Fe K-edge for Fe foil, FeMn-SAC@NC, Fe/Mn-SAC@NC and Fe-SAC@NC. Fit in *R* space with the magnitude and the imaginary at Fe K-edge for (e) FeMn-SAC@NC and (f) Fe/Mn-SAC@NC. (g) FT of the k^2-weighted EXAFS spectra at Mn K-edge for Mn foil, FeMn-SAC@NC, Fe/Mn-SAC@NC and Mn-SAC@NC. Fit in *R* space with the magnitude and the imaginary at Mn K-edge for (h) FeMn-SAC@NC and (i) Fe/Mn-SAC@NC.

(Table S3 in the ESM). By contrast, at this overpotential, the reference catalysts of Fe/Mn-SAC@NC, Fe-SAC@NC and Mn-SAC@NC only exhibited a FE_{CO} of 78%, 72% and 44%, respectively, far below that of FeMn-SAC@NC, which highlighted the synergistic effect between those atomically dispersed Fe and Mn in a short distance in boosting CO_2RR. Moreover, the turnover frequency (TOF) for CO production per single-metal-site of FeMn-SAC@NC based on the total metal loadings was also calculated and compared with those recently reported heteronuclear SACs (Fig. 3(c)). Apparently, this value is among the most active SACs in CO_2RR, and even comparable with some state-of-the-art Au catalysts. The stability of FeMn-SAC@NC towards CO_2RR was further tested at a small overpotential of 320 mV. The FeMn-SAC@NC exhibited a stable FE_{CO} and *j* after a continuous test in 24 h, demonstrating the remarkable cycle durability (Fig. 3(d)). After CO_2RR performance, the morphology of FeMn-SAC@NC remained stable without any visible metal nanoparticles (Fig. S14 in the ESM).

Furthermore, Tafel analysis was carried out to get insights into the reaction kinetics for CO_2RR of these as-prepared catalysts [61, 62]. As present in Fig. 3(e), Fe/Mn-SAC@NC, Fe-SAC@NC, Mn-SAC@NC and NC displayed a Tafel slope of 105, 156, 185 and 317 mV·dec^{-1}, respectively. Obviously, the first electron transfer for CO_2 activation is the rate-determining step for the entire CO_2RR process on these catalysts [63]. By comparison, a Tafel slope of 62 mV·dec^{-1} was calculated on FeMn-SAC@NC. The much smaller Tafel slope highlighted the faster initial electron transfer to a CO_2 molecule for CO_2 activation on FeMn-SAC@NC than on the rest catalysts [64]. Besides, the fast electron transfer for FeMn-SAC@NC was also testified by its lower interfacial charge-transfer resistance (R_{ct}) of 57.2 Ω than Fe/Mn-SAC@NC (101.6 Ω), Fe-SAC@NC (106.3 Ω), Mn-SAC@NC (155.5 Ω) and NC (323.0 Ω) (Fig. S15 in the ESM). In this sense, stabilization for the COOH* intermediate was to a large extent improved on FeMn-SAC@NC than on the other catalysts, and such enhanced stabilization of COOH* significantly accelerated CO production especially at low overpotentials. Moreover, the electrochemical active surface areas (ECSA) of these as-synthesized catalysts were also calculated via measuring their corresponding double-layer capacitances (Figs. S16 and S17 and Table S4 in the ESM). Obviously, FeMn-SAC@NC and Fe/Mn-SAC@NC exhibited a similar ECSA, implying that both catalysts consisted of a comparable number of active sites. Taking

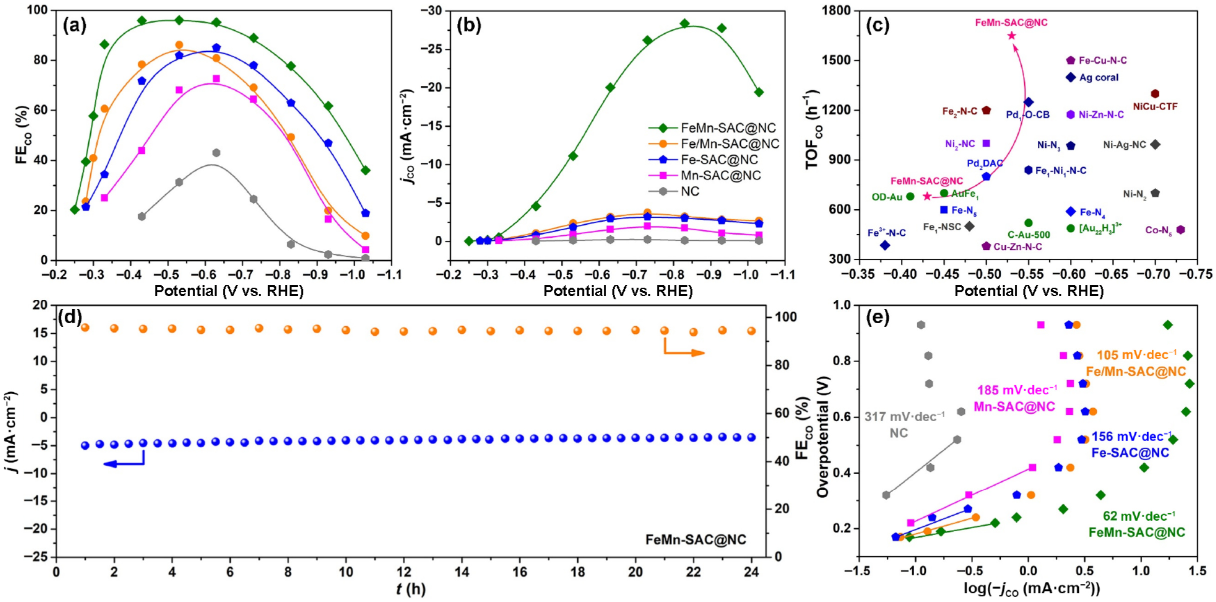

Figure 3 (a) FE_{CO} and (b) j_{CO} of FeMn-SAC@NC (olive), Fe/Mn-SAC@NC (orange), Fe-SAC@NC (blue), Mn-SAC@NC (pink) and NC (gray). (c) TOFs of FeMn-SAC@NC and some reference single-atom, dual-atom and state-of-the-art Au catalysts for CO production. (d) Stability test of FeMn-SAC@NC for CO_2RR in CO_2-saturated 0.5 M $KHCO_3$ electrolyte at −0.43 V vs. RHE. (e) Tafel slope of FeMn-SAC@NC, Fe/Mn-SAC@NC, Fe-SAC@NC, Mn-SAC@NC and NC.

into consideration the distinct difference in the CO_2RR activity between these two catalysts, the inter-site distance between single Fe and Mn atoms in the nitrogen-doped carbon matrix was supposed to largely promote the instinct activity of these single-metal-atom centers.

To illustrate how the inter-site distance between single Fe and Mn atoms affected the CO_2RR performance, density functional theory (DFT) calculations were further performed. A graphene layer containing single Fe atom, single Mn atom, and dual single Fe and Mn atoms with different proximity, namely, FeMn-SAC@NC, FeMn(1)-SAC@NC, FeMn(2)-SAC@NC and FeMn(3)-SAC@NC was built (the number in bracket represented the number of horizontal axial carbon atoms between the adjacent Fe and Mn atoms, see Fig. S18 in the ESM for details). According to the EXAFS fitting results, each Fe and Mn atom in these models was coordinated by four N atoms and one hydroxyl group. In general, electrocatalytic CO_2RR to CO is comprised of reaction pathways in the sequence of CO_2, CO_2*, COOH*, CO* and CO, among which the first electron transfer step for the generation of COOH* (CO_2* + H^+ + e^- → COOH*) is normally regarded as the rate-determining step [65]. The reaction Gibbs free energy (ΔG) of this step on the metal-free NC sample showed a value of 2.31 eV, indicative of a high energy barrier for CO_2 activation (Fig. S19 in the ESM). In contrast, incorporation of single Fe or Mn atom into the graphene lattice decreased the barrier of this step to 1.15 and 1.46 eV, respectively, implying that the presence of single atom site enhanced CO_2 activation and COOH* formation (Fig. 4(a)). Interestingly, when single Fe and Mn atoms coexisted in the graphene lattice, the reaction energy for *COOH formation on Fe decreased sharply and was dependent on the proximity between Fe and Mn. Specifically, as single Fe and Mn sites were getting closer, the required ΔG for COOH* formation decreased from 1.10 eV (FeMn(3)-SAC@NC) to 1.00 eV (FeMn(2)-SAC@NC), 0.81 eV (FeMn(1)-SAC@NC) and 0.63 eV (FeMn-SAC@NC). Obviously, the highest activity for *COOH formation was achieved when single Mn atom was located at the neighboring site of Fe along with the highest energy barrier for HER (Fig. S20 in the ESM). At the same time, the reaction barrier for COOH* formation on Fe was much lower than the value on Mn in the same model catalyst, manifesting the promoted CO_2RR reactivity of Fe by the surrounding Mn (Fig. 4(a) and Fig. S21 in the ESM). However, since the reaction barriers for COOH* formation on Mn sites of all model catalysts were similar and much higher than those on Fe, such promotion on Mn by Fe was trivial. For the second electron transfer step (COOH* + H^+ + e^- → CO* + H_2O), it was an exothermic process over all model catalysts. However, FeMn-SAC@NC showed the lowest reaction barrier for CO* desorption among all the Fe-containing catalysts. Such a phenomenon highlighted that the neighboring Mn site induced a much weaker interaction between Fe and CO*, leading to fast CO desorption and active site generation. Hence, the facilitation for COOH* generation and CO* desorption renders FeMn-SAC@NC with neighboring Fe and Mn sites highly active for CO_2RR at low overpotentials.

Electronic property analysis, including density of state (DOS), partial DOS (PDOS) and charge density difference were further carried out to figure out the underlying factors controlling the conspicuous differences in CO_2RR performance over these model catalysts. It is speculated that the *d* orbital of Fe or Mn interact with the *p* orbital of C atom to stabilize the COOH* intermediate via formation of metal–carbon bond over the catalyst [66]. Thus, *d* electron distribution at the Fermi level is preferable for such interaction and accounting for the high activity for COOH* formation. As for the DOS results, FeMn-SAC@NC with neighboring Fe and Mn sites has the most abundant distribution of *d* electrons from Fe at Fermi level compared to the rest catalysts with Fe and Mn in a long distance, as well as Fe-SAC@NC and Mn-SAC@NC (Figs. 4(e)–4(j)). Since the oxidation states of Fe for Fe-SAC@NC, FeMn-SAC@NC and bulk Fe_2O_3 that were measured by Bader charge analysis were +1.21e, +1.16e and +1.50e, respectively, the reduced oxidation state of Fe in FeMn-SAC@NC due to the presence of neighboring Mn in the system was further supported. As present in Fig. 4(k), such electronic alteration of Fe in FeMn-SAC@NC influenced the adsorption properties of COOH*. More electrons were contributed from the Fe center in FeMn-SAC@NC

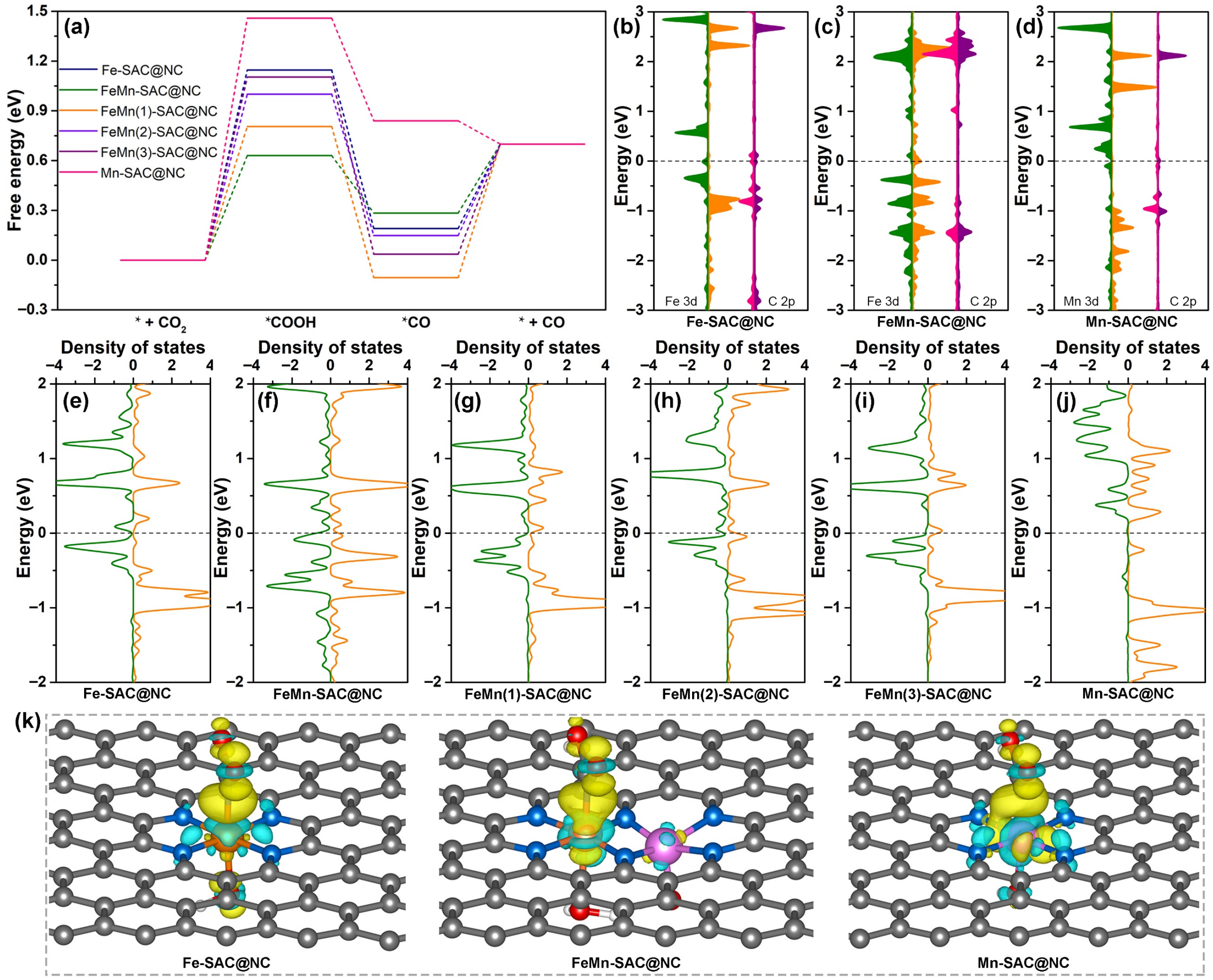

Figure 4 (a) Calculated free energy diagrams for CO_2RR to CO on single Fe site for Fe-SAC@NC, FeMn-SAC@NC, FeMn(1)-SAC@NC, FeMn(2)-SAC@NC and FeMn(3)-SAC@NC as well as on single Mn site for Mn-SAC@NC. DOS of the orbital interaction for (b) Fe-SAC@NC and (c) FeMn-SAC@NC between Fe 3d and C 2p of COOH* and for (d) Mn-SAC@NC between Mn 3d and C 2p of COOH*. DOS of (e) Fe-SAC@NC, (f) FeMn-SAC@NC, (g) FeMn(1)-SAC@NC, (h) FeMn(2)-SAC@NC, (i) FeMn(3)-SAC@NC and (j) Mn-SAC@NC (orange: Fe spin up; olive: Fe spin down). (k) Differential charge density of Fe-SAC@NC, FeMn-SAC@NC and Mn-SAC@NC (yellow: accumulation; cyan: depletion; isosurface value = 0.015 e$Å^{-3}$).

to bond with COOH*, resulting in a significant amount of electron density accumulated around the Fe–C bond. In contrast, the stabilization of COOH* on Fe-SAC@NC and Mn-SAC@NC needed electrons donation from four adjacent N atoms by means of their weak hybridization ability. Hence, the neighboring Mn site, despite not directly active for CO_2 activation itself, transfers electrons to the adjacent Fe site for stabilization of the key COOH* intermediate. This was also evidenced by the PDOS analysis, from which a shift of the *p* orbital for COOH* downward the Fermi level was observed on FeMn-SAC@NC as compared to that on Fe-SAC@NC and Mn-SAC@NC, indicative of the strong interaction between Fe and C (Figs. 4(b)–4(d)). Accordingly, the boosted electron interactions increased the stability of COOH* on the Fe site of FeMn-SAC@NC, leading to a low energy barrier for COOH* formation, and the electron enriched Fe center induced by neighboring Mn endows FeMn-SAC@NC highly active for CO_2RR to CO compared to the rest counterparts.

3 Conclusions

In summary, we have successfully synthesized a series of nitrogen-doped carbon supported Fe and Mn heteronuclear single atom catalysts with different Fe and Mn inter-site distance via a silica-templated isolation approach, and tested them in electrocatalytic CO_2RR for CO production. We proved that the inter-site distance between atomically dispersed Fe and Mn sites controlled the CO_2RR performance and the catalyst with atomic Fe and Mn sites in close proximity exhibited the highest CO_2RR performance, with a high FE_{CO} (96%), an outstanding durability (24 h) at a low overpotential of 320 mV, and superior kinetics for CO_2RR with a Tafel slope of only 62 mV·dec^{-1}. Such CO_2RR performance surpassed most of the reported atomically dispersed electrocatalysts and even comparable to state-of-the-art AuNPs. Experimental analysis together with DFT calculation suggested that single Mn atom at the neighboring site of Fe increased the electronic density of Fe, which dramatically reduced the energy barriers for COOH* production as well as CO* desorption on Fe, and hence boosted the CO_2RR performance at low overpotentials. These findings present the scientific comprehension of the correlation between the inter-site distance of atomic sites and CO_2RR performance, and pave a new avenue to precisely control single-atom sites on carbon support for highly active and selective electrocatalysts.

Electronic Supplementary Material: Supplementary material (further details of experimental procedures for the preparation, characterization, and catalytic testing of catalysts; details of DFT calculations; additional TEM, XRD, Raman, XPS, and EXAFS results of the catalysts; additional catalytic results including LSV, FE(H_2), electrochemical impedance spectroscopy (EIS), cyclic voltammetry (CV) and double-layer capacitance (C_{dl}) data; additional DFT calculation results including model structures, Gibbs energy graphs for CO_2RR and HER.) is available in the online version of this article at https://doi.org/10.26599/NR.2025.94907249.

Data availability

All data needed to support the conclusions in the paper are presented in the manuscript and the Electronic Supplementary Material. Additional data related to this paper may be requested from the corresponding author upon request.

Acknowledgements

This work was supported by National Natural Science Foundation of China (Nos. 22478419, 22102080, and 221011150), Key Project of National Natural Science Foundation of China (No. U22B20149) and Science Foundation of China University of Petroleum (Beijing) (No. ZX20230067). The authors acknowledge the Dutch Organization for Scientific Research (NWO) for access to the Dutch national e-infrastructure (Nos. EINF-4693 and EINF-6899). The authors thank the BL14W1 station in Shanghai Synchrotron Radiation Facility (SSRF) and the 1W1B station in Beijing Synchrotron Radiation Facility (BSRF) for XAFS test.

Declaration of competing interest

The authors declare that they have no known competing financial interests or personal relationships that could have appeared to influence the work reported in this paper.

Author contribution statement

X. H. S.: Supervision, formal analysis, review & editing, project administration, funding acquisition. B. Y. Z.: Methodology, visualization, writing manuscript. Q. L.: Formal analysis, methodology. J. J. J.: Software, formal analysis. C. L. Y.: Formal analysis, visualization, writing manuscript. G. Q. C.: Formal analysis. Z. C. Z.: Formal analysis, methodology. J. Z.: Methodology. J. H. B.: Methodology. G. N. L.: Formal analysis, software, writing manuscript. C. M. X.: Methodology. All the authors have approved the final manuscript.

Use of AI statement

None.

References

[1] Wu, Y. S.; Jiang, Z.; Lu, X.; Liang, Y. Y.; Wang, H. L. Domino electroreduction of CO_2 to methanol on a molecular catalyst. *Nature* **2019**, *575*, 639–642.

[2] Yang, Y.; Louisia, S.; Yu, S. B.; Jin, J.; Roh, I.; Chen, C. B.; Fonseca Guzman, M. V.; Feijóo, J.; Chen, P. C.; Wang, H. S. et al. *Operando* studies reveal active Cu nanograins for CO_2 electroreduction. *Nature* **2023**, *614*, 262–269.

[3] Kim, J. Y. T.; Sellers, C.; Hao, S. Y.; Senftle, T. P.; Wang, H. T. Different distributions of multi-carbon products in CO_2 and CO electroreduction under practical reaction conditions. *Nat. Catal.* **2023**, *6*, 1115–1124.

[4] Sun, X. H.; Suarez, A. I. O.; Meijerink, M.; van Deelen, T.; Ould-Chikh, S.; Zečević, J.; de Jong, K. P.; Kapteijn, F.; Gascon, J. Manufacture of highly loaded silica-supported cobalt Fischer–Tropsch catalysts from a metal organic framework. *Nat. Commun.* **2017**, *8*, 1680.

[5] Wezendonk, T. A.; Sun, X. H.; Dugulan, A. I.; van Hoof, A. J. F.; Hensen, E. J. M.; Kapteijn, F.; Gascon, J. Controlled formation of iron carbides and their performance in Fischer–Tropsch synthesis. *J. Catal.* **2018**, *362*, 106–117.

[6] Li, S. J.; Dong, X.; Wu, G. F.; Song, Y. F.; Mao, J. N.; Chen, A. H.; Zhu, C.; Li, G. H.; Wei, Y. H.; Liu, X. H. et al. Ampere-level CO_2 electroreduction with single-pass conversion exceeding 85% in acid over silver penetration electrodes. *Nat. Commun.* **2024**, *15*, 6101.

[7] Liu, M. J.; Zhan, L. S.; Wang, Y. C.; Zhao, X.; Wu, J.; Deng, D. N.; Jiang, J. B.; Zheng, X. R.; Lei, Y. P. Achieving integrated capture and reduction of CO_2: A promising electrocatalyst. *J. Mater. Sci. Technol.* **2023**, *165*, 235–243.

[8] Sun, X. H.; Wang, R. M.; Ould-Chikh, S.; Osadchii, D.; Li, G. N.; Aguilar, A.; Hazemann, J. L.; Kapteijn, F.; Gascon, J. Structure–activity relationships in metal organic framework derived mesoporous nitrogen-doped carbon containing atomically dispersed iron sites for CO_2 electrochemical reduction. *J. Catal.* **2019**, *378*, 320–330.

[9] Zhang, Y.; Mu, X. Q.; Liu, Z. Y.; Zhao, H. Y.; Zhuang, Z. C.; Zhang, Y. F.; Mu, S. C.; Liu, S. L.; Wang, D. S.; Dai, Z. H. Twin-distortion modulated ultra-low coordination PtRuNi-O_x catalyst for enhanced hydrogen production from chemical wastewater. *Nat. Commun.* **2024**, *15*, 10149.

[10] Zhao, X.; Feng, Q. G.; Liu, M. J.; Wang, Y. C.; Liu, W.; Deng, D. N.; Jiang, J. B.; Zheng, X. R.; Zhan, L. S.; Wang, J. X. et al. Built-in electric field promotes interfacial adsorption and activation of CO_2 for C_1 products over a wide potential window. *ACS Nano* **2024**, *18*, 9678–9687.

[11] Mu, X. Q.; Liu, S. L.; Zhang, M. Y.; Zhuang, Z. C.; Chen, D.; Liao, Y. R.; Zhao, H. Y.; Mu, S. C.; Wang, D. S.; Dai, Z. H. Symmetry-broken Ru nanoparticles with parasitic Ru-Co dual-single atoms overcome the volmer step of alkaline hydrogen oxidation. *Angew. Chem., Int. Ed.* **2024**, *63*, e202319618.

[12] Shang, W. Z.; Liu, W.; Cai, X. B.; Hu, J. W.; Guo, J. Y.; Xin, C. C.; Li, Y. H.; Zhang, N. T.; Wang, N.; Hao, C. et al. Insights into atomically dispersed reactive centers on g-C_3N_4 photocatalysts for water splitting. *Adv. Powder Mater.* **2023**, *2*, 100094.

[13] Monteiro, M. C. O.; Dattila, F.; Hagedoorn, B.; García-Muelas, R.; López, N.; Koper, M. T. M. Absence of CO_2 electroreduction on copper, gold and silver electrodes without metal cations in solution. *Nat. Catal.* **2021**, *4*, 654–662.

[14] Mariano, R. G.; Kang, M.; Wahab, O. J.; McPherson, I. J.; Rabinowitz, J. A.; Unwin, P. R.; Kanan, M. W. Microstructural origin of locally enhanced CO_2 electroreduction activity on gold. *Nat. Mater.* **2021**, *20*, 1000–1006.

[15] Yang, Z. K.; Zhao, C. M.; Qu, Y. T.; Zhou, H.; Zhou, F. Y.; Wang, J.; Wu, Y. E.; Li, Y. D. Trifunctional self-supporting cobalt-embedded carbon nanotube films for ORR, OER, and HER triggered by solid diffusion from bulk metal. *Adv. Mater.* **2019**, *31*, 1808043.

[16] Wu, Y. H.; Chen, C. J.; Yan, X. P.; Sun, X. F.; Zhu, Q. G.; Li, P. S.; Li, Y. M.; Liu, S. J.; Ma, J. Y.; Huang, Y. Y. et al. Boosting CO_2 electroreduction over a cadmium single-atom catalyst by tuning of the axial coordination structure. *Angew. Chem., Int. Ed.* **2021**, *60*, 20803–20810.

[17] Martini, A.; Hursán, D.; Timoshenko, J.; Rüscher, M.; Haase, F.; Rettenmaier, C.; Ortega, E.; Etxebarria, A.; Roldan Cuenya, B. Tracking the evolution of single-atom catalysts for the CO_2 electrocatalytic reduction using *operando* X-ray absorption

spectroscopy and machine learning. *J. Am. Chem. Soc.* **2023**, *145*, 17351–17366.

[18] Sun, X. H.; Wang, L. L.; Lan, X. Y.; Lu, Q.; Tuo, Y.; Ye, C. L.; Wang, D. S.; Xu, C. M. Positively charged nickel-sulfur dual sites for efficient CO_2 electroreduction reaction. *Appl. Catal. B: Environ.* **2024**, *342*, 123389.

[19] Bai, Z. Q.; Zhang, W. H.; Liu, Y. F. Enhanced nitrogen electroreduction performance by the reorganization of local coordination environment of supported single atom on N(O)-dual-doped graphene. *Nano Res.* **2023**, *16*, 9099–9106.

[20] Liu, T. Y.; Wang, Y.; Li, Y. F. Can metal-nitrogen-carbon single-atom catalysts boost the electroreduction of carbon monoxide. *JACS Au* **2023**, *3*, 943–952.

[21] Dong, W. F.; Zhang, N.; Li, S. X.; Min, S. X.; Peng, J.; Liu, W. Y.; Zhan, D. P.; Bai, H. C. A Mn single atom catalyst with Mn–N_2O_2 sites integrated into carbon nanosheets for efficient electrocatalytic CO_2 reduction. *J. Mater. Chem. A* **2022**, *10*, 10892–10901.

[22] Wang, S. C.; Zhang, M. Y.; Mu, X. Q.; Liu, S. L.; Wang, D. S.; Dai, Z. H. Atomically dispersed multi-site catalysts: Bifunctional oxygen electrocatalysts boost flexible zinc-air battery performance. *Energy Environ. Sci.* **2024**, *17*, 4847–4870.

[23] Zhou, Y. Z.; Zhou, Q.; Liu, H. J.; Xu, W. J.; Wang, Z. X.; Qiao, S. C.; Ding, H. H.; Chen, D. L.; Zhu, J. F.; Qi, Z. M. et al. Asymmetric dinitrogen-coordinated nickel single-atomic sites for efficient CO_2 electroreduction. *Nat. Commun.* **2023**, *14*, 3776.

[24] Zhang, W.; Liu, D.; Liu, T.; Ding, C. L.; Chen, T.; Li, Y. M.; Liu, X. K.; Wang, L.; Li, C. L.; He, J. F. et al. Coordinately unsaturated nickel single atom electrocatalyst for efficient CO_2 conversion. *Nano Res.* **2023**, *16*, 10873–10880.

[25] Pan, F. P.; Zhang, H. G.; Liu, K. X.; Cullen, D.; More, K.; Wang, M. Y.; Feng, Z. X.; Wang, G. F.; Wu, G.; Li, Y. Unveiling active sites of CO_2 reduction on nitrogen-coordinated and atomically dispersed iron and cobalt catalysts. *ACS Catal.* **2018**, *8*, 3116–3122.

[26] Zhu, S. Q.; Li, T. H.; Cai, W. B.; Shao, M. H. CO_2 electrochemical reduction As probed through infrared spectroscopy. *ACS Energy Lett.* **2019**, *4*, 682–689.

[27] Mohd Adli, N.; Shan, W. T.; Hwang, S.; Samarakoon, W.; Karakalos, S.; Li, Y.; Cullen, D. A.; Su, D.; Feng, Z. X.; Wang, G. F. et al. Engineering atomically dispersed FeN_4 active sites for CO_2 electroreduction. *Angew. Chem., Int. Ed.* **2021**, *60*, 1022–1032.

[28] Chen, Y.; Zhao, J.; Pan, X. L.; Li, L.; Yu, Z. N.; Wang, X. D.; Ma, T. Y.; Lin, S.; Lin, J. Tuning the inter-metal interaction between Ni and Fe atoms in dual-atom catalysts to boost CO_2 electroreduction. *Angew. Chem., Int. Ed.* **2024**, *63*, e202411543.

[29] Mu, X. Q.; Yu, M.; Liu, X. Y.; Liao, Y. R.; Chen, F. J.; Pan, H. Z.; Chen, Z. Y.; Liu, S. L.; Wang, D. S.; Mu, S. C. High-entropy ultrathin amorphous metal-organic framework-stabilized Ru(Mo) dual-atom sites for water oxidation. *ACS Energy Lett.* **2024**, *9*, 5763–5770.

[30] Li, L.; Dai, X. Y.; Lu, M. C.; Guo, C. F.; Wabaidur, S. M.; Wu, X. L.; Lou, Z. R.; Zhong, Y. J.; Hu, Y. Electron-enriched single-Pd-sites on g-C_3N_4 nanosheets achieved by *in-situ* anchoring twinned Pd nanoparticles for efficient CO_2 photoreduction. *Adv. Powder Mater.* **2024**, *3*, 100170.

[31] Wang, Y.; Wu, J.; Tang, S. H.; Yang, J. R.; Ye, C. L.; Chen, J.; Lei, Y. P.; Wang, D. S. Synergistic Fe–Se atom pairs as bifunctional oxygen electrocatalysts boost low-temperature rechargeable Zn-air battery. *Angew. Chem., Int. Ed.* **2023**, *62*, e202219191.

[32] Zhang, Y. F.; Liu, L. S.; Li, Y. X.; Mu, X. Q.; Mu, S. C.; Liu, S. L.; Dai, Z. H. Strong synergy between physical and chemical properties: Insight into optimization of atomically dispersed oxygen reduction catalysts. *J. Energy Chem.* **2024**, *91*, 36–49.

[33] Zhang, J. W.; Zeng, G. M.; Chen, L. L.; Lai, W. C.; Yuan, Y. L.; Lu, Y. F.; Ma, C.; Zhang, W. H.; Huang, H. W. Tuning the reaction path of CO_2 electroreduction reaction on indium single-atom catalyst: Insights into the active sites. *Nano Res.* **2022**, *15*, 4014–4022.

[34] Liu, Z.; Liu, Y. X.; Zhang, J. Q.; Cao, T.; Sun, Z. Y.; Liu, J. Z.; Shang, H. S. Asymmetrically coordinated single atom Cu catalyst with unsaturated C–Cu–N structure for CO_2 reduction to CO. *Nano Res.* **2024**, *17*, 3911–3918.

[35] Wang, Y.; Ma, F. Y.; Zhang, G. Q.; Zhang, J. W.; Zhao, H.; Dong, Y. M.; Wang, D. S. Precise synthesis of dual atom sites for electrocatalysis. *Nano Res.* **2024**, *17*, 9397–9427.

[36] Zhan, X. Y.; Fan, X. Y.; Li, W. X.; Tan, X. Y.; Robertson, A. W.; Muhammad, U.; Sun, Z. Y. Coupled metal atomic pairs for synergistic electrocatalytic CO_2 reduction. *Matter* **2024**, *7*, 4206–4232.

[37] Yao, Z. B.; Cheng, H.; Xu, Y. F.; Zhan, X. Y.; Hong, S.; Tan, X. Y.; Wu, T. S.; Xiong, P.; Soo, Y. L.; Li, M. M. J. et al. Hydrogen radical-boosted electrocatalytic CO_2 reduction using Ni-partnered heteroatomic pairs. *Nat. Commun.* **2024**, *15*, 9881.

[38] Jin, Z. Y.; Li, P. P.; Meng, Y.; Fang, Z. W.; Xiao, D.; Yu, G. H. Understanding the inter-site distance effect in single-atom catalysts for oxygen electroreduction. *Nat. Catal.* **2021**, *4*, 615–622.

[39] Xia, W.; Xie, Y. J.; Jia, S. Q.; Han, S. T.; Qi, R. J.; Chen, T.; Xing, X. Q.; Yao, T.; Zhou, D. W.; Dong, X. et al. Adjacent copper single atoms promote C–C coupling in electrochemical CO_2 reduction for the efficient conversion of ethanol. *J. Am. Chem. Soc.* **2023**, *145*, 17253–17264.

[40] Liang, Z.; Song, L. P.; Sun, M. Z.; Huang, B. L.; Du, Y. P. Tunable CO/H_2 ratios of electrochemical reduction of CO_2 through the Zn-Ln dual atomic catalysts. *Sci. Adv.* **2021**, *7*, eabl4915.

[41] Zhu, J. B.; Xiao, M. L.; Ren, D. Z.; Gao, R.; Liu, X. Z.; Zhang, Z.; Luo, D.; Xing, W.; Su, D.; Yu, A. P. et al. Quasi-covalently coupled Ni–Cu atomic pair for synergistic electroreduction of CO_2. *J. Am. Chem. Soc.* **2022**, *144*, 9661–9671.

[42] Cui, T. T.; Wang, Y. P.; Ye, T.; Wu, J.; Chen, Z. Q.; Li, J.; Lei, Y. P.; Wang, D. S.; Li, Y. D. Engineering dual single-atom sites on 2D ultrathin N-doped carbon nanosheets attaining ultra-low-temperature zinc-air battery. *Angew. Chem., Int. Ed.* **2022**, *61*, e202115219.

[43] Jiao, L.; Zhu, J. T.; Zhang, Y.; Yang, W. J.; Zhou, S. Y.; Li, A. W.; Xie, C. F.; Zheng, X. S.; Zhou, W.; Yu, S. H. et al. Non-bonding interaction of neighboring Fe and Ni single-atom pairs on MOF-derived N-doped carbon for enhanced CO_2 electroreduction. *J. Am. Chem. Soc.* **2021**, *143*, 19417–19424.

[44] Zhang, M. Y.; Zhou, D. Y.; Mu, X. Q.; Wang, D. S.; Liu, S. L.; Dai, Z. H. Regulating the critical intermediates of dual-atom catalysts for CO_2 electroreduction. *Small* **2024**, *20*, 2402050.

[45] Hao, J. C.; Zhu, H.; Zhao, Q.; Hao, J. C.; Lu, S. L.; Wang, X.; Duan, F.; Du, M. L. Interatomic electron transfer promotes electroreduction CO_2-to-CO efficiency over a CuZn diatomic site. *Nano Res.* **2023**, *16*, 8863–8870.

[46] Chen, Y. J.; Ji, S. F.; Wang, Y. G.; Dong, J. C.; Chen, W. X.; Li, Z.; Shen, R. A.; Zheng, L. R.; Zhuang, Z. B.; Wang, D. S. et al. Isolated single iron atoms anchored on N-doped porous carbon as an efficient electrocatalyst for the oxygen reduction reaction. *Angew. Chem., Int. Ed.* **2017**, *56*, 6937–6941.

[47] Sun, X. H.; Olivos-Suarez, A. I.; Osadchii, D.; Romero, M. J. V.; Kapteijn, F.; Gascon, J. Single cobalt sites in mesoporous N-doped carbon matrix for selective catalytic hydrogenation of nitroarenes. *J. Catal.* **2018**, *357*, 20–28.

[48] Xiao, Z. H.; Zhao, L.; Yu, Z. Q.; Zhang, M. X.; Li, S. P.; Zhang, R. H.; Ayub, M.; Ma, X. L.; Ning, G. Q.; Xu, C. M. Multilayered graphene endowing superior dispersibility for excellent low temperature performance in lithium-ion capacitor as both anode and cathode. *Chem. Eng. J.* **2022**, *429*, 132358.

[49] Xiao, Z. H.; Chen, Z.; Sun, Y. K.; Li, T.; Zhao, L.; Li, Z. C.; Yu, Z. Q.; Gao, Z. F.; Ma, X. L.; Xu, C. M. Spherical nano-graphite anode derived from electrochemical stripping for high performance Li-ion capacitors. *Chem. Eng. J.* **2023**, *474*, 145623.

[50] To, J. W. F.; He, J. J.; Mei, J. G.; Haghpanah, R.; Chen, Z.; Kurosawa, T.; Chen, S. C.; Bae, W. G.; Pan, L. J.; Tok, J. B. H. et al. Hierarchical N-doped carbon as CO_2 adsorbent with high CO_2 selectivity from rationally designed polypyrrole precursor. *J. Am. Chem. Soc.* **2016**, *138*, 1001–1009.

[51] Li, J. J.; Xia, W.; Tang, J.; Gao, Y.; Jiang, C.; Jia, Y. N.; Chen, T.; Hou, Z. F.; Qi, R. J.; Jiang, D. et al. Metal-organic framework-derived graphene mesh: A robust scaffold for highly exposed Fe–N_4 active sites toward an excellent oxygen reduction catalyst in acid media. *J. Am. Chem. Soc.* **2022**, *144*, 9280–9291.

[52] Yang, J.; Liu, W. G.; Xu, M. Q.; Liu, X. Y.; Qi, H. F.; Zhang, L. L.; Yang, X. F.; Niu, S. S.; Zhou, D.; Liu, Y. F. et al. Dynamic behavior of single-atom catalysts in electrocatalysis: Identification of Cu-N_3 as an active site for the oxygen reduction reaction. *J. Am. Chem. Soc.* **2021**, *143*, 14530–14539.

[53] Hu, X. L.; Luo, G.; Zhao, Q. N.; Wu, D.; Yang, T. X.; Wen, J.; Wang, R. H.; Xu, C. H.; Hu, N. Ru single atoms on N-doped carbon by spatial confinement and ionic substitution strategies for high-performance Li–O_2 batteries. *J. Am. Chem. Soc.* **2020**, *142*, 16776–16786.

[54] Mills, P.; Sullivan, J. L. A study of the core level electrons in iron and its three oxides by means of X-ray photoelectron spectroscopy. *J. Phys. D: Appl. Phys.* **1983**, *16*, 723–732.

[55] Wan, X.; Liu, Q. T.; Liu, J. Y.; Liu, S. Y.; Liu, X. F.; Zheng, L. R.; Shang, J. X.; Yu, R. H.; Shui, J. L. Iron atom-cluster interactions increase activity and improve durability in Fe–N–C fuel cells. *Nat. Commun.* **2022**, *13*, 2963.

[56] Ramesh, K.; Chen, L. W.; Chen, F. X.; Liu, Y.; Wang, Z.; Han, Y. F. Re-investigating the CO oxidation mechanism over unsupported MnO, Mn_2O_3 and MnO_2 catalysts. *Catal. Today* **2008**, *131*, 477–482.

[57] Sun, H. X.; Zaera, F. Chemical vapor deposition of manganese metallic films on silicon oxide substrates. *J. Phys. Chem. C* **2012**, *116*, 23585–23595.

[58] Zhang, Q.; Tsai, H. J.; Li, F. H.; Wei, Z. M.; He, Q. Y.; Ding, J.; Liu, Y. H.; Lin, Z. Y.; Yang, X. J.; Chen, Z. Y. et al. Boosting the proton-coupled electron transfer via Fe–P atomic pair for enhanced electrochemical CO_2 reduction. *Angew. Chem., Int. Ed.* **2023**, *62*, e202311550.

[59] Feng, J. Q.; Gao, H. S.; Zheng, L. R.; Chen, Z. P.; Zeng, S. J.; Jiang, C. Y.; Dong, H. F.; Liu, L. C.; Zhang, S. J.; Zhang, X. P. A Mn-N_3 single-atom catalyst embedded in graphitic carbon nitride for efficient CO_2 electroreduction. *Nat. Commun.* **2020**, *11*, 4341.

[60] Guo, Z.; Xie, Y. B.; Xiao, J. D.; Zhao, Z. J.; Wang, Y. X.; Xu, Z. M.; Zhang, Y.; Yin, L. C.; Cao, H. B.; Gong, J. L. Single-atom Mn–N_4 site-catalyzed peroxone reaction for the efficient production of hydroxyl radicals in an acidic solution. *J. Am. Chem. Soc.* **2019**, *141*, 12005–12010.

[61] Zhuansun, M. J.; Liu, Y.; Lu, R. H.; Zeng, F.; Xu, Z. Y.; Wang, Y.; Yang, Y. Y.; Wang, Z. Y.; Zheng, G. F.; Wang, Y. H. Promoting CO_2 electroreduction to multi-carbon products by hydrophobicity-induced electro-kinetic retardation. *Angew. Chem., Int. Ed.* **2023**, *62*, e202309875.

[62] Li, S. J.; Dong, X.; Zhao, Y. H.; Mao, J. N.; Chen, W.; Chen, A. H.; Song, Y. F.; Li, G. H.; Jiang, Z.; Wei, W. et al. Chloride ion adsorption enables ampere-level CO_2 electroreduction over silver hollow fiber. *Angew. Chem., Int. Ed.* **2022**, *61*, e202210432.

[63] Chang, X. X.; Li, J.; Xiong, H. C.; Zhang, H. C.; Xu, Y. F.; Xiao, H.; Lu, Q.; Xu, B. J. C–C coupling is unlikely to be the rate-determining step in the formation of C_{2+} products in the copper-catalyzed electrochemical reduction of CO. *Angew. Chem. , Int. Ed.* **2022**, *61*, e202111167.

[64] Gu, J.; Hsu, C. S.; Bai, L. C.; Chen, H. M.; Hu, X. L. Atomically dispersed Fe^{3+} sites catalyze efficient CO_2 electroreduction to CO. *Science* **2019**, *364*, 1091–1094.

[65] Vijay, S.; Ju, W.; Brückner, S.; Tsang, S. C.; Strasser, P.; Chan, K. Unified mechanistic understanding of CO_2 reduction to CO on transition metal and single atom catalysts. *Nat. Catal.* **2021**, *4*, 1024–1031.

[66] Zhao, Y. F.; Jiang, W. J.; Zhang, J. Q.; Lovell, E. C.; Amal, R.; Han, Z. J.; Lu, X. Y. Anchoring sites engineering in single-atom catalysts for highly efficient electrochemical energy conversion reactions. *Adv. Mater.* **2021**, *33*, 2102801.